Modeling the 2D behavior of dry-stone retaining walls by a fully discrete element method

Oetomo, J.J. , Vincens, E. , Dedecker, F. and Morel, J. C.

Original citation & hyperlink:
Oetomo, J.J. , Vincens, E. , Dedecker, F. and Morel, J. C. (2015) Modeling the 2D behavior of dry-stone retaining walls by a fully discrete element method. International Journal for Numerical and Analytical Methods in Geomechanics, volume 40 (7): 1099-1120
http://dx.doi.org/10.1002/nag.2480

DOI 10.1002/nag.2480
ISSN 0363-9061
ESSN 1096-9853

Publisher: Wiley

Modeling the 2D behavior of drystone retaining walls by a fully discrete element method

J. J. Oetomo[1], E. Vincens[1], F. Dedecker[2], J-C. Morel[3]

[1] University of Lyon, LTDS, UMR CNRS 5513, Ecole Centrale de Lyon, 36 Avenue Guy de Collongue, 69134 Ecully Cedex, France

[2] Itasca Consultants, S.A.S., 64 Chemin des Mouilles, 69134 Ecully Cedex, France

[3] Coventry University, Faculty of Engineering, Environment and Computing, School of Energy, Construction and Environment, Centre for Low Impact Buildings, Priory Street, CV1 5FB, United Kingdom

Abstract

The dry-stone retaining walls (DSRW) have been tipped as a promising solution for sustainable development. However, before recently, their behavior is relatively obscure. In this study, DEM approach was applied to simulate the plane strain failure of these walls. A commercial DEM package (PFC2D^{TM}) was used throughout this study. The authors used a fully discrete approach, thus both the wall and the backfill were modeled as discrete elements. The methodology for obtaining the micromechanical parameters was discussed in detail; this includes the three mechanical sub-systems of DSRWs: wall, backfill and interface. The models were loaded progressively until failure, and then the results were compared with the full-scale experimental results where the walls were loaded respectively with hydrostatic load and backfill. Despite its complexity and its intensive calculation time, DEM model can then be used to validate a more simplified approach.

Keywords

Dry-stone, retaining wall, discrete element method, plane strain failure

Notations

R_n	wall-backfill normalized roughness
AR	grain aspect ratio
ϕ_b^g	block-block global friction angle
ϕ_b^l	block-block local friction angle
ϕ_g^g	backfill internal friction angle
ϕ_{gc}^g	backfill critical friction angle
ϕ_g^l	backfill local friction angle
n_0	backfill porosity
ϕ_i^g	wall-backfill interface global friction angle
ϕ_i^l	wall-backfill interface local friction angle

1. Introduction

Many geotechnical related problems usually involve large and localized deformations, material discontinuities and complex evolution of soil behavior. With the aim of simulating the real yet complicated phenomena, discrete element method (DEM) is nowadays acknowledged to be a compelling approach to simulate these problems.

Since introduced by Cundall and Strack in late 70s [1], discrete element method or sometimes denoted distinct element method has gone from promising to important technique in the study of granular materials; this includes a wide range of applications from powder technology to environmental and geotechnical sciences. The examples of DEM application in geotechnical problems include the following: rockfill dams stability [2], protection against rock fall impact [3] and landslide hazard analysis [4].

In this paper, DEM is used to study a particular geotechnical structure: dry-stone retaining walls (DSRWs). Dry-stone walling is an ancient technique, where stones are selected then used with very minimal shaping to build a structure. They are hand-placed following a certain know-how that provides sufficient stiffness and hardiness to the structure. It should be underlined that stone structures can be classified as dry-stone structures if they are built without mortar. It means that the structural stability of such structures relies exclusively on the friction and interlocking between blocks. The typical geometry of DSRWs is shown in Figure 1, wall height is typically between 2-4 m, but can rise up to 10 m high [5].

During the past and until the late 19th century, DSRWs were extensively used to counter slope erosion, creating terraces for agricultural cultures. But they were also used either along highways to connect cities or to support the highways themselves in mountains. These structures generated the least interest when more efficient bonded masonry or reinforced concrete structures were preferred during the 20th century. Even if this heritage is still visible, most of them possessed various degree of deterioration due to the time effect. A survey by Odent [6] showed that approximately 18% of retaining walls in France are classified as DSRWs, while O'Reilly et al. [7] estimated that there is around 9000 km of such walls in Great Britain.

The current rehabilitation process of the DSRWs as well as the construction of a new one is largely hampered by a very limited scientific knowledge regarding these structures. This can be explained by the complex behavior of DSRWs, where each block can move independently. This means that the dry-stone walls might deform extensively before failure due to blocks sliding. This is also the primary reason why DEM approach seems more suitable to model the behavior of DSRW towards failure than more established continuum approaches.

The earliest study of dry-stone wall can be traced back to early 19th century, where Burgoyne [8] built four full-scale DSRWs at Kingstown (now Dún Laoghaire, Ireland). His full-scale experimental campaign was valuable and has been repeatedly used by researchers to validate their own studies [9,10]; however his experiments can be qualified as qualitative experiments and lack of some essential data such as the soil friction angle and the contact friction between blocks, as well as some more thorough information: for example, the construction technique and the deformation behavior during the loading phase.

Recent full-scale experimental campaigns have been done at least by two research groups, one from ENTPE, France [11,12,13] and another one from the University of Bath, UK [14]. Our study is based on two experimental campaigns conducted by the group from ENTPE; hereafter they will be referred as case A and B.

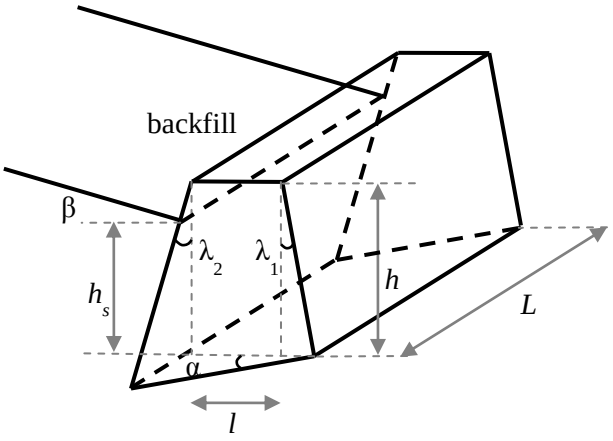

Notation:
h = height
L = length
l = thickness
λ_1 = wall batter
λ_2 = wall counter-slope
α = joint inclination
β = backfill slope
h_s = backfill height

Figure 1: Geometry of dry-stone retaining walls (DSRWs).

DSRWs' failure mode is related to the loading mode supported by the structure. Figure 2 shows two types of plane DSRWs, namely: (1) Slope retaining wall and; (2) Road retaining wall. The first one is simply backfilled with soil, and in the configuration where the wall is plane, sufficiently long and uniformly loaded, the failure mode would be tied with a plain-strain condition. The failure modes of DSRWs in plain-strain condition are well-known: they are either sliding or toppling failures (Figure 3a and Figure 3b) [15]. The second one submits a load combination: the soil weight and the impact of a vehicle weight, creating a bulged/belly shape. This mode of failure is a true three-dimensional failure mode.

Recently, the results from experimental campaigns for case A and B structures have been compared with an analytical approach called "yield design" [16,17,18] (an upper-bound approach), yielding a good agreement. However this method can only predict the ultimate strength of DSRWs and does not give access to the strain field which can be critical: for example when very large strains can alter the roadway integrity in the case of road retaining walls.

In this study, we prospect the ability of DEM solution to address the 2D failure behavior of slope DSRW. We will particularly highlight advantages and drawbacks of this method but also stress the difficulties for a correct description of phenomena observed on site.

2. Experimental campaigns

In both cases A and B, the height and the length of the walls are similar and are uniformly loaded along their inward face, which provides a failure compatible with a plane strain condition (Figure 2a).

In case A (Figure 4a), a simple hydrostatic load was used. In order to apply a hydrostatic load, an impermeable PVC membrane was installed at the inward wall face [11]. Though simple, the DEM modeling of this system will provide a validation of the wall model itself which is a first stage of the verification step. Five different heights were studied and two types of stones (limestone and schist) were selected. More details can be found in [11].

For case B (Figure 4b), four DSRWs of 2 m height were loaded with a rounded-elongated gravel. These grains were discharged from a container and were progressively deposited under gravity, forming a natural angle of repose for the backfill. Different technologies for the construction of the DSRW were used and more details can be found in [12].

(a)

(b)

Figure 2: Two types of DSRWs: (a) Slope retaining wall (b) Road retaining wall. Photo credit: Paul McCombie.

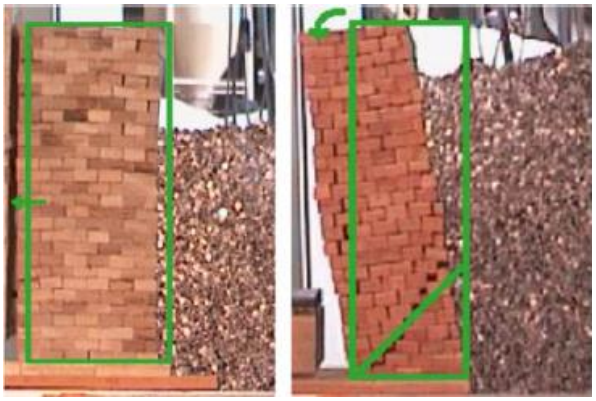

(a) (b)

Figure 3: Plane-strain failure of scale down DSRW: (a) sliding (b) toppling [15].

(a) (b)

Figure 4: Experimental campaigns loaded with: (a) Hydrostatic pressure (case A) [11]; (b) Backfill load (case B) [12].

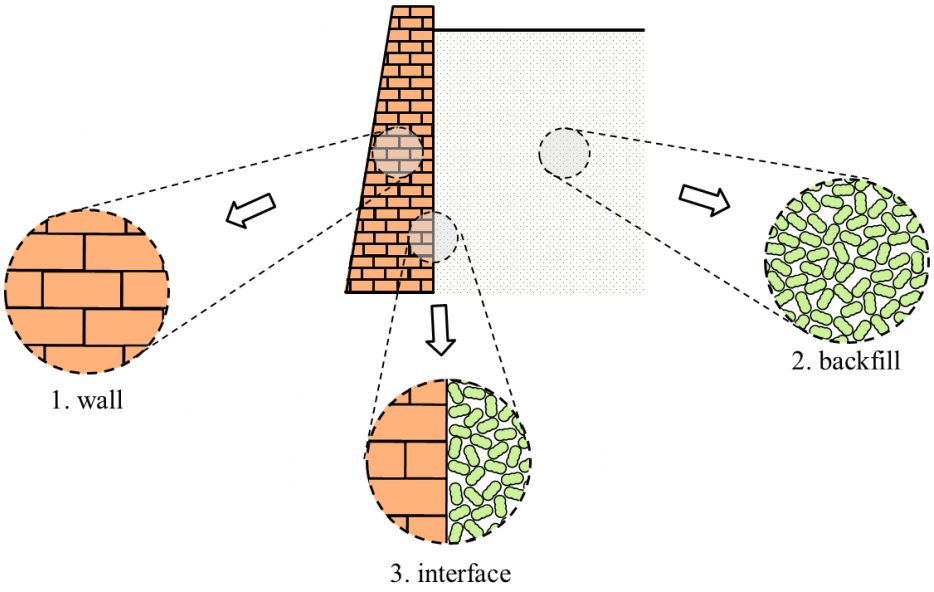

Figure 5: Three sub-systems for DSRWs.

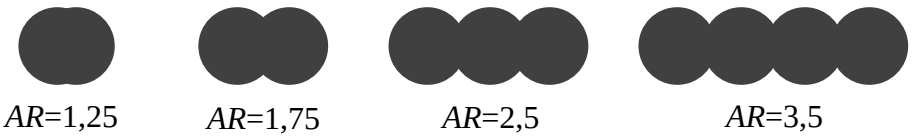

Figure 6: Grains with various aspect ratios (*AR*).

3. Modelling of DSRWs with a particle-based method

The slope retaining wall basically consists of three distinct mechanical sub-systems (Figure 5): (1) the dry-stone wall; (2) the soil or backfill; and (3) the wall-backfill interface. Since the failure can be seen as a plain strain mode, a two-dimensional modeling will be performed.

The DEM package used here is PFC2D^{TM} (Particle Flow Code) developed by ITASCA, based on an explicit solution method. The basic elements are rigid disks with deformable contacts. This code was used because of its flexibility for the creation of different objects with different shapes. Indeed, the user has the possibility to glue rigid circular bodies together generating more complex bodies. The approach considered in this work is different from previous numerical studies [9,10,19,20] which coupled a discrete method for blocks and a continuum model for backfill.

At each time-step, the calculation runs in alternate between contact-force law and law of motion. The constitutive law at micro scale is the heart of the particle based simulation. The simplest contact law that can be selected consists of a spring, where the force magnitude is calculated as follows:

$$\boldsymbol{F_n = k_n\, u_n} \qquad \textbf{(1)}$$

$$\boldsymbol{\Delta F_s = -k_s\, \Delta u_s} \qquad \textbf{(2)}$$

The normal stiffness k_n is a secant modulus, relating the total normal displacement u_n to the normal force F_n. On the other hand, the shear stiffness k_s is a tangent modulus relating the incremental shear displacement Δu_s to the increment of the tangential force ΔF_s. This stiffness should be sufficiently high to avoid excessive interpenetration, which may lead to an overrepresentation of the elastic behavior. In the same time, it is preferable to use a relatively small value as it reduces the critical time step. The shear stiffness is compounded at each time step and it may lead to sliding failure following Coulomb's friction law:

$$\boldsymbol{|F_s^t = F_s^{t-1} + \Delta F_s| \leq \mu\, F_n} \qquad \textbf{(3)}$$

with μ the local friction angle.

3.1 Model geometry

PFC2D^{TM} models the movement and interaction of stressed assemblies of rigid circular particles. However, a more complex shape can be created as an assembly of the circular particles. The final assembly can then be treated as a rigid or a deformable body.

The DSRWs consist of two different materials: stone blocks and backfill grains (Figure 5). By using particle based simulation, both should be created using a certain number of disks. By their very nature, stone blocks have a high resistance, even higher than concrete. Thus, stone blocks can be modeled as rigid bodies with deformable contacts. Disks with diameter between 8-11 mm have been used to create stone blocks. The average disk size is small enough to generate shapes similar to actual stone blocks but not too small to provide a relative roughness at the interface wall-soil compatible to what was observed in case B experiments.

Few studies have already shown that grain elongation affects the critical friction angle of a soil [21,22,23,24,25]. Therefore, in the model, the backfill grains shape will be characterized by an aspect ratio *AR* which used a value, as close as possible to the real grains. As an illustration, Figure 6 shows grains with various aspect ratios. The calibration of the aspect ratio for the study will be covered in section 4.2.

3.2 Mechanical interactions

For both types of contact, grain-grain and block-grain, contacts are deformable and a linear contact law is used. This is the default contact law in PFC2D^{TM} whereas sliding occurs following Coulomb's friction law, perpendicular to the direction of the contact vector. Both normal and tangential stiffnesses must be defined. In this work, for the sake of simplicity, the tangential stiffness will be equal to the normal stiffness.

Regarding the contact laws between block-block, between backfill grains or at the wall-backfill interface, different points must be arisen. For the first system, the contact is identified through individual contacts between the disks forming the outer shape of the blocks (Figure 7a or Figure 7b). Each individual contact has its own plane of contact with its own direction. A primary study showed that the block macro-roughness creates a fluctuation of results around an average value. For example, the fluctuation of the maximum mobilized friction angle throughout an interface shear test was found as high as ±5°. Since this fluctuation may alter the understanding of the DSRW behavior towards failure, another contact law was chosen.

In this work, we consider a smooth-joint contact law [26] which basically removes the block geometrical roughness. This contact law is similar to the linear contact law except that: (1) the contact plane direction is the same at each disk contact and (2) sliding takes place along a given contact area A (or length in 2D model). The following formulations are used to calculate the contact forces for smooth-joint contacts:

$$\boldsymbol{F_n^t = F_n^{t-1} + k_n' A\, u_n} \qquad (4)$$

$$\boldsymbol{F_s^t = F_s^{t-1} - k_s' A\, \Delta u_s} \qquad (5)$$

By default, the surface area A (or length in 2D) of a smooth joint contact is computed using the minimum radius between two particles in contact. Due to the physical roughness, the total surface area of contacts can be greater than the plane block surface area; hence A is multiplied by the ratio between the plane surface area of the block and the total surface area of contacts between two blocks. A corresponding correction applies in 2D (i.e. length instead of surface). In Figure 7b, the contact plane at each contact is equal to the horizontal plane which can be considered as the average contact plane between the two blocks. Consequently, this law is similar to a homogenized contact law. The applied friction coefficient takes into account both the macro and the micro roughness as typically measured in a direct shear test.

The contact stiffnesses can be identified through compression or shear tests. Since high values may penalize computation times, smaller values may be chosen if the phenomena that want to be observed are not excessively affected by this modification. For the block-block contact, a primary parametric study showed that the behavior of the wall towards failure is not modified if the smooth-joint contact stiffnesses (k_n' and k_s') are dropped to a value of 10^8 Pa/m. For the backfill grain-grain contact, the comparison between the evolution of the mobilized friction angle throughout the actual triaxial tests and simulated biaxial tests led us to choose linear contact stiffnesses (k_n and k_s) that equal to 5.10^7 Pa. For the wall-backfill interface, a default value of linear contact stiffnesses of 5.10^7 Pa will be taken.

In addition to the friction at contacts, viscous damping can also be introduced to dissipate the kinetic energy. Damping forces F_D act to oppose motion and can be projected to the normal and tangential direction at contacts, formulated as follows:

$$\boldsymbol{F_D = c\,|V|} \qquad (6)$$

Where c is the damping constant and V is the relative velocity at the contact. In PFC, instead of the damping constant, the critical damping ratio ζ is used as the input parameter:

$$c = \zeta\, c_{crit} \qquad (7)$$

In general, the introduction of viscous damping does not affect the outcome of quasi-static simulations such as those involved in this work (i.e. incrementally loaded DSRW). However, as the backfill grains were generated layer-by-layer and stabilized under gravity, grains may impact other grains before they came to rest. A critical damping ratio ζ_n=0.5 and ζ_t=0.0 at both normal and tangential direction was introduced.

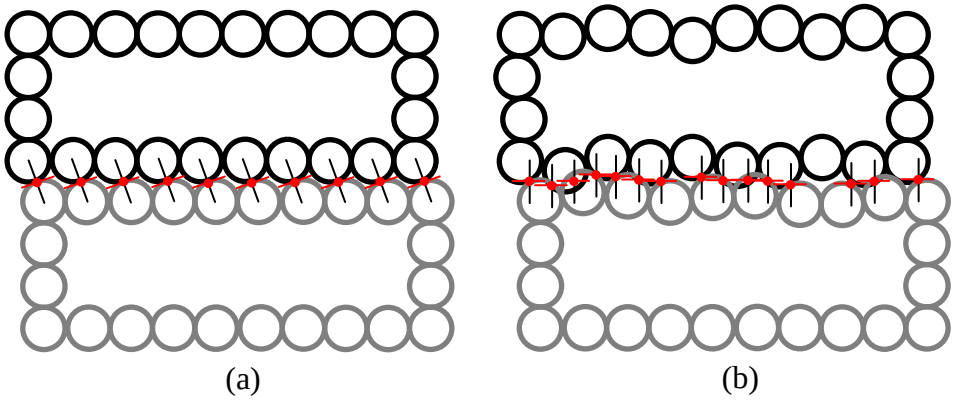

Figure 7: Block model with: (a) Linear contact (b) Smooth-joint contact.

4. Assessment of micromechanical parameters

In view of the DEM approach, the macroscopic behavior of a system is the results of the interaction of individual bodies where a direct path between the micro-behavior and the macro-behavior is difficult to trace. Then, generally, the micromechanical properties are calibrated using a trial-and-error method in order for the global behavior of the system to be produced. Three sub-systems are individually studied to identify the micro-properties: the wall, the backfill and the wall-backfill interface.

In the previous section, we pointed out that the smooth-joint contact law for a block-block contact is similar to a homogenized law. Thus, the local friction angle of the block-block contact $\phi_b^{\,l}$ is supposed to be equal to the global friction angle $\phi_b^{\,g}$ determined by a tilt test.

4.1 Backfill: Identifying the grains mechanical parameters

The round fluvial gravel used in case B experiments has a grading comprised between 8 and 16 mm (Figure 8). The way the gravel deposited to create the backfill explains the state of density that corresponds to a loose state. As such, a unit weight of 14.9 kN/m^3 for the gravel was identified for a loose case in the full scale experiments. Three triaxial tests have been performed in a non-conventional triaxial apparatus to satisfy the statement of the Representative Elementary Volume [12]. These three tests correspond to confining pressures of 20 kPa, 50 kPa and 100 kPa. The critical state was difficult to identify through these tests, nevertheless the angle of repose of the backfill was reported to be close to 32°. From these tests, and stating that an average representative

mean stress for the backfill is equal to 35 kPa, an internal friction angle of 37.7° and a dilatancy angle of 8° for the backfill have been identified.

Figure 8: Granular backfill used in the experiments by Colas [12].

We propose an identification process for the backfill local parameters in two phases. First, we state that the angle of repose of the backfill is close to the critical friction angle which does not strictly hold true. Indeed, the material in both states share a common loose state but the angle of repose corresponds to a very low confining stress whereas the angle at critical state is generally identified through triaxial tests performed with confining stresses greater or equal to 100kPa.

The critical state friction angle only depends on the following properties: grading, D_{50}, sphericity and angularity of grains [21,22,23,24,25] and finally the local friction angle between grains [27,28]. All these properties are usually denoted as intrinsic properties. In the DEM model, the grain-grain contact is supposed to be linear elastic and associated to a Coulomb's law. To limit the size of the smaller particles (and then the computation time), the grading is supposed to be linear and set to the interval of 10-16 mm. Two properties of the modeled grains are able to participate in the development of shearing resistance at critical state: the grain elongation and the local friction angle. Consequently, the identification process of these two properties will be carried out using a trial-and-error method.

A proper 2D modeling of an actual 3D granular material should involve a certain variety of aspect ratios since a 2D modeling is expected to represent in some way the main features observed in a cross-sectional view of the actual material. Nevertheless, for the sake of simplicity this option was not chosen, and a constant aspect ratio for the grains has been considered in this work. Then, series of biaxial simulations have been performed on an assembly of granular material having the proper grading with a given aspect ratio and a given local friction angle between grains. For a given box size, the number of grains in the box varies according to the grain aspect ratio. Even for the strongly elongated grain AR=2.5, more than 2250 grains have been used so that the size of the sample can be considered as a Representative Elementary Volume.

The grains were poured in a rigid box of 75x150 cm^2 whereas its drop height equals to five times of the grain maximum size (D_{max}). The sample creation process is then compatible with the process of backfill generation on site. After reaching the equilibrium, a compression test with a confinement stress of 35 kPa and a loading strain rate of 10^{-3}/s was simulated. We plot in Figure 9a, the friction angle at critical state versus different local friction angles (between grains) for an aspect ratio of 1.75. One can note that it was impossible, in that case, to reach the critical friction angle of 32°. Using an aspect ratio of 2.5 (Figure 9b), we slightly increase the friction angle at critical state. It was found that having a large aspect ratio could be a problem since it induces strong local heterogeneities involving local arching effects. Then, we decided not to increase the aspect ratio of

grains greater than 2.5 for a local friction angle ϕ_g^l of 45°. Such a high local friction may not hold a physical meaning, however, this value has been already used to model the behavior of elongated aggregates in a rockfill dam [29].

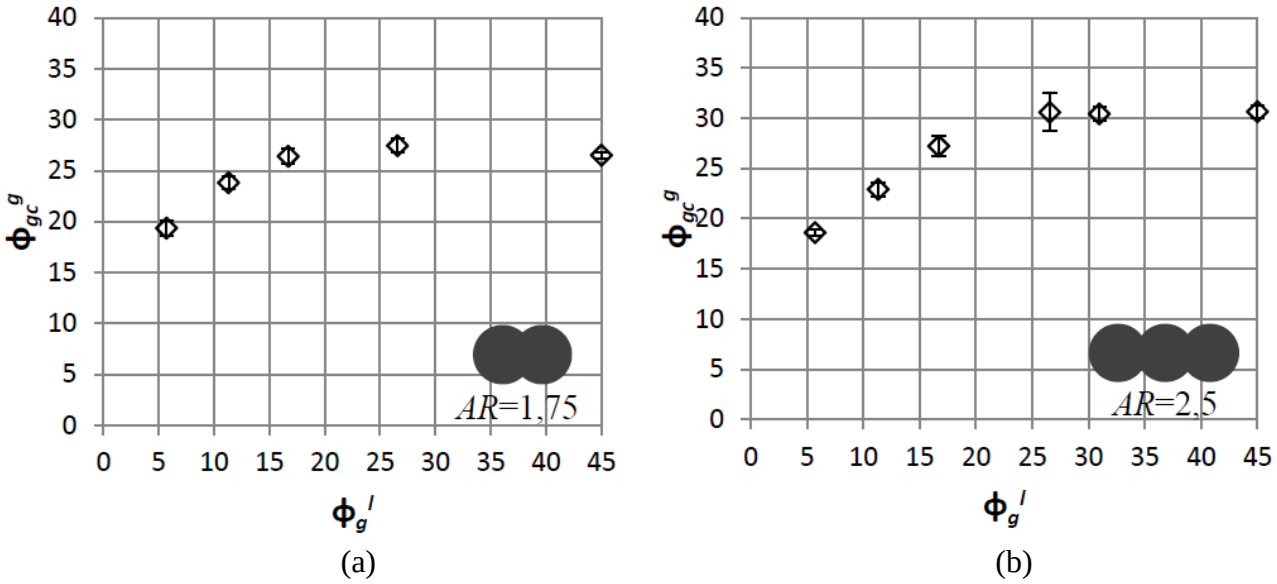

Figure 9: Effect of grain-grain local friction angle ϕ_g^l to the grain resistance at critical state ϕ_{gc}^g for the following aspect ratios: (a) AR=1.75 (b) AR=2.5.

The second stage of the identification process allows the internal friction of the backfill to be retrieved. This friction angle is associated to the maximum shearing resistance of the granular material. For a given material, this maximum shearing resistance mainly depends on density [30]. A trial-and-error method is also used to identify the initial porosity of a numerical sample able to lead throughout a shearing test to an internal friction angle ϕ_g^g of 37.7°.

Smaller initial porosities of sample are made from a very loose state (initial porosity of around 0.27 for a local friction angle ϕ_g^l of 45°) by decreasing temporarily and gradually ϕ_g^l while a new equilibrium state is searched. Generally, the sample is in a static equilibrium when the ratio between the maximum unbalanced force to the maximum contact force is smaller than 10^{-4}. Once the desired porosity is obtained, the local friction angle ϕ_g^l is set to a value previously calibrated (45°).

Thereafter, simulations of compression phase are performed and the internal friction angle is then deduced. Figure 10 depicts the values for the internal friction angle obtained through simulations of biaxial tests for different initial sample porosities. The compatible initial porosity n_0 for the expected backfill internal friction angle ϕ_g^g of 37.7° is approximately equal to 0.22.

Finally, for the selected parameters (AR=2.5, ϕ_g^l=45° and n_0=0.22), the evolution of the stress ratio q/p (q and p are respectively the second invariant and the first invariant of the stress tensor) for the numerical sample is compared to the triaxial tests performed on the actual backfill material in Figure 11a. Two curves are given for the actual triaxial tests, corresponding to a confining stress of 20 kPa and 50 kPa, respectively. We remind that the representative confining stress considered for the backfill was taken equal to 35 kPa.

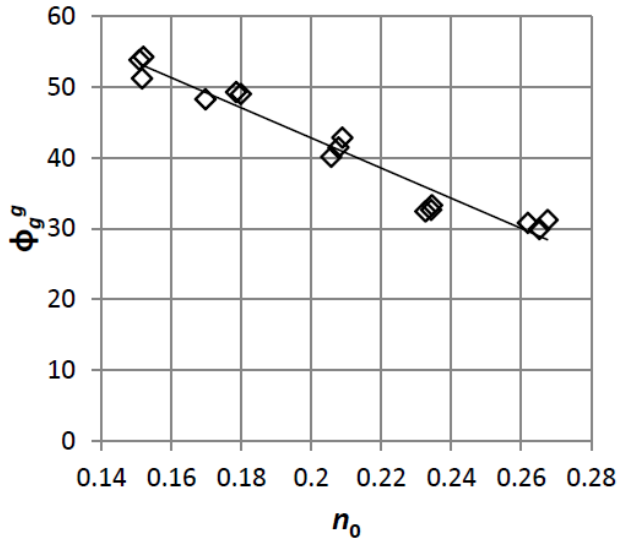

Figure 10: Effect of initial porosity (n_0) to the internal friction angle of sample ϕ_g^g, with AR=2.5 and ϕ_g^l=45°.

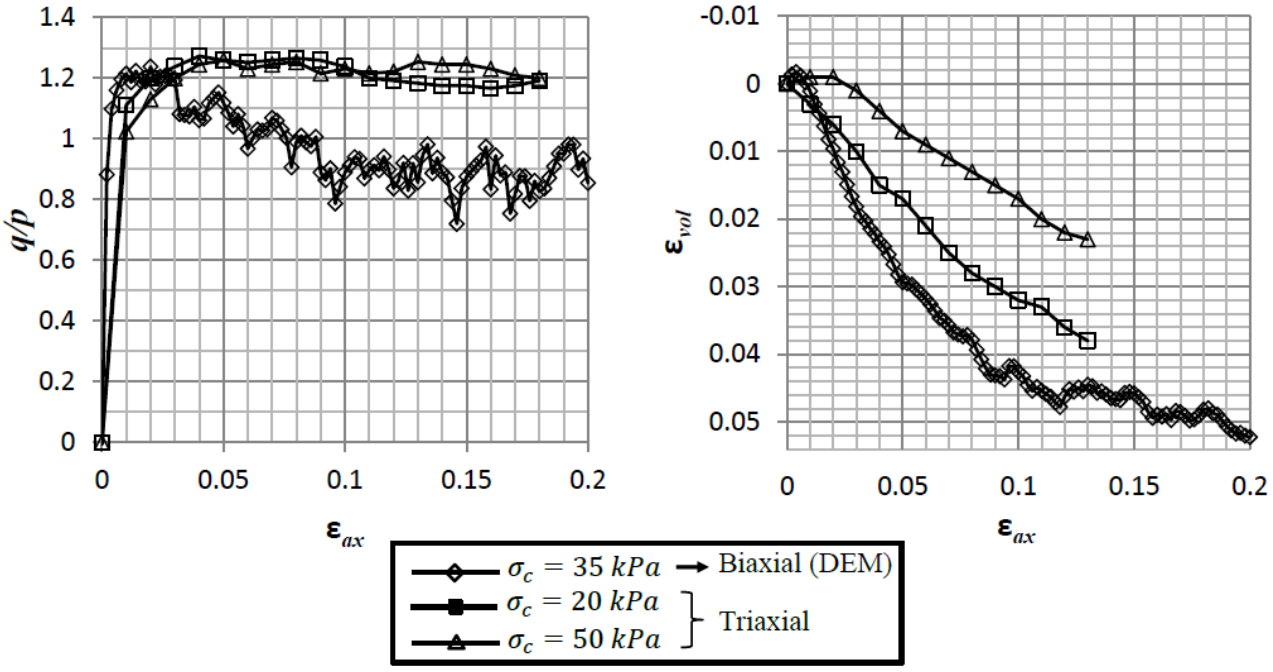

Figure 11: Evolution of the stress ratio *q/p* for the biaxial DEM simulation and the actual triaxial tests.

The stress path evolution versus the peak of resistance fairly reproduces the increase of mobilized friction within the real material. Nevertheless, the numerical sample exhibits a strong softening which is almost unnoticeable for the actual backfill material. This feature implies that, given the intrinsic parameter of the numerical sample (i.e. aspect ratio for grains and the local friction angle ϕ_g^l), the sample with an initial porosity of 0.22 holds the behavior of a dense sample. It is not the case for the actual material which holds the behavior of a loose material. Only the modification of the intrinsic properties of grains (increase of the local friction angle or of the aspect ratio) will reduce the strong softening in the numerical sample. However, an increase of ϕ_g^l will not greatly reduce the softening since its value is definitely already very high and an increase of the aspect ratio would create other biases in the simulations. For example, we can mention the emergence of strong local heterogeneities in terms of porosities even greater at the contact between backfill and wall. It

would lead fewer contact points between the backfill grains and the wall which would reduce the quality of stress transfer between the two wall sub-systems.

The corresponding evolution of the volumetric deformations is depicted in Figure 11b. This figure emphasizes a further limit of a two-dimensional modeling to simulate a real three-dimensional problem. In two-dimensional samples, dilative patterns are generally overrepresented [31]. In fact, while in 3D, rotations and displacements can take place in all the directions, for a given shear stress increment, the movements within a 2D material are bound to take place in a 2D-single plane for translations and around a single axis for rotations. Dilatancy is even more noticeable as the aspect ratio of grains equals to 2.5.

4.2 Backfill-wall interface

Three different definitions of the interfaces between the backfill and the wall exist. The first one is related to the true boundary of wall-backfill which is discrete by nature. It corresponds to the contact points between the backfill grains and the wall blocks. It holds true for DEM modeling where particles from the backfill will be in contact with the particles forming the outer surfaces of the wall blocks. On the other hand, the interface between a granular soil and a structure can also be identified as a zone within the soil where shear stresses concentrate when the whole system is submitted to a shearing process. In the case of a wall-backfill interface, this interface definition portrays a zone within the backfill and close to the wall where shear stresses concentrate.

This zone is usually identified with an equivalent device of a direct shear box [32]. From direct shear test, the interface width was found within the range of 10-12D_{50} (D_{50} is the diameter of the 50% finer) [33].

Finally, one can identify the interface as the zone where wall affects the particle arrangement, inducing a porosity increase in the vicinity of the wall. Earlier studies shown that the interface thickness extends for $2D_{100}$ from the wall [34,35] for uniform materials or for a distance greater than $5D_{50}$ in the case of more broadly graded materials [36].

The mechanical behavior of a soil-structure interface depends on the normalized roughness R_n of the interface (Figure 12) [37]. This latter property is defined as the ratio of the geometrical roughness of the structure R_{max} to the D_{50} of the soil grains. If R_n is small (typically smaller than 0,02), the interface behaves as a smooth interface, where the stress path represents an elastic perfectly plastic material [38] without any dilative behavior. The interface is able to develop some degree of dilatancy if R_n increases up to 0.1 and then holds a transitional behavior towards a true rough interface. When the normalized roughness is greater than 0.1, the interface exhibits an elastoplastic behavior with hardening and may experience some degree of softening towards a critical state [38,39]. An interface, qualified as a rough interface, holds then a behavior comparable to the soil, with an influence of density.

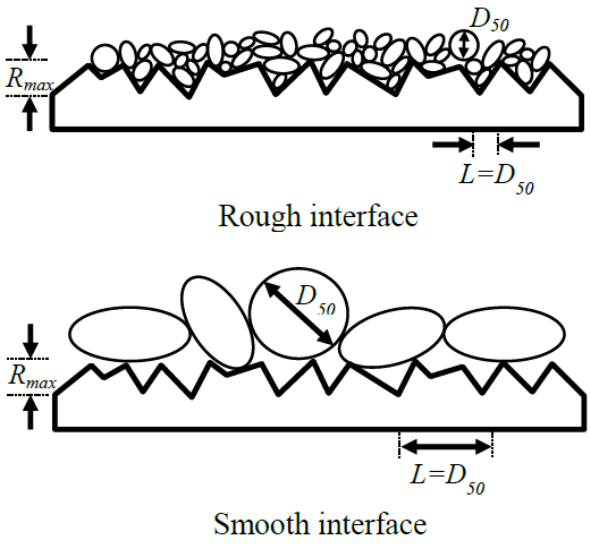

Figure 12: Comparison between rough and smooth interface [32,39].

The average normalized roughness along the interface has been estimated to 1.5 from observation on-site. Thus the interface can be considered as a rough interface. There is no other information available from the full scale experiments on DSRWs concerning the interface. For determining the critical backfill height using the yield design method, Colas et al. [18] stated that the internal friction angle of the backfill-wall interface ϕ_i^g is equal to the backfill internal friction angle ϕ_g^g. In fact, this statement corresponds to the European Code for Geotechnical Works (EUROCODE 7) for concrete-soil interface in the case of in-situ concrete. At this stage, it seems relevant to extrapolate this recommendation to the case of DSRWs.

Since backfill particles are in contact with the wall blocks, a specific property for this contact must be identified. A linear elastic contact associated to a Coulomb's law is adopted and the normal and tangential stiffness of the block-backfill grain contact will be equal to 5.10^7 Pa as indicated in section 3.2. Finally, a local friction angle ϕ_i^l shall be defined. The desired value will be obtained by means of a Constant Normal Load (CNL) test which is a typical test to identify the soil-structure interface behavior. A trial-and-error method was used to identify ϕ_i^l.

Figure 13 sketches the numerical model developed to reproduce a CNL test. The inward wall surface (horizontal surface with tainted blue particles) at the bottom in Figure 13 was simplified to a continuous surface assuming that the discontinuity between adjacent wall blocks does not influence the results. The rigid box has been filled with the backfill grains previously defined (section 4.2) put under gravity. In order to obtain an initial porosity of 0.22 as identified in section 4.2, ϕ_g^l was gradually and temporarily decreased until the desired density is found, then ϕ_g^l is reverted to 45°. A rigid flat wall closes the top of the box. This wall can move vertically in order to keep a constant vertical stress (equal to 35 kPa) all along the CNL test. No friction was applied between the backfill particles and the rigid walls of the box. The lateral walls of the box were fixed, a horizontal velocity of 5.10^{-4} m/s is applied to the bottom wall. The size of the sample is 0.90 m length and 0.50 m height and it is composed of 925 backfill particles. The box is sufficiently wide to have a fairly large number of contacts between the wall and the backfill grains, hence reducing the fluctuation in measurement at the interface.

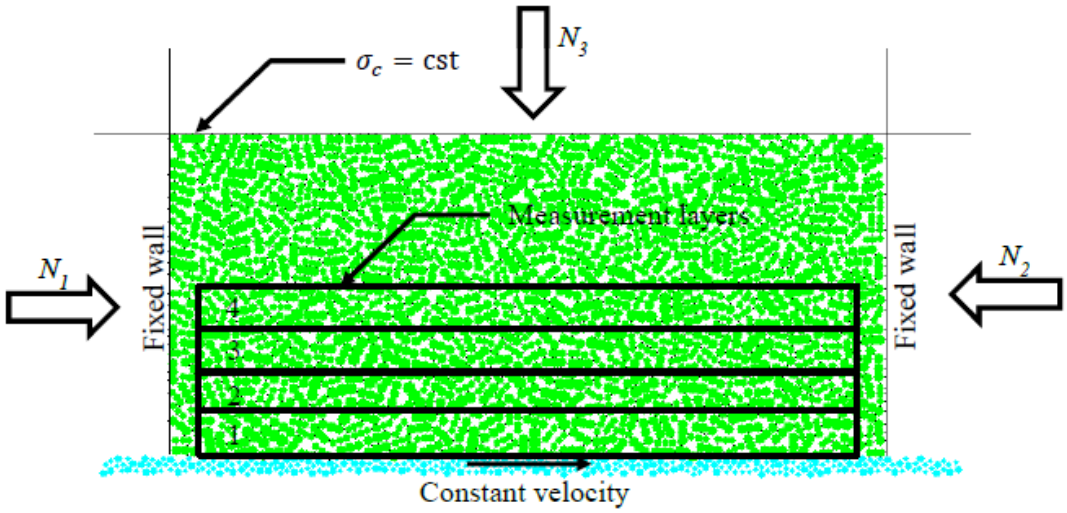

Figure 13: Model of CNL direct shear test.

In an actual CNL test, the information at the interface can only be obtained by means of an inverse method, in the sense that the measurements are performed at global sample scale. More details about the methodology can be found in [40]. The DEM allows us to have direct information within the sample. The lower part of the sample is then divided into 4 layers of $3D_{50}$ thick each with a full-length discarding the zone close to the vertical walls. The state of stress is monitored and a mobilized friction angle is computed in each layers. More details on the formulation used to calculate the homogenized stress in measurement layers can be found in [41]. Since the sample is actually one realization of a random process, four shear tests have been simulated for a given value of the local interface friction angle ϕ_i^l.

Figure 14 shows the evolution of the mobilized friction angle measured inside the first layer (layer 1 in Figure 14 and denoted "in" in Figure 15), which represents the behavior of the backfill-wall interface when shearing. On the other hand, the curves with dashed lines are associated to results derived from the use of an inverse method similar that would be used in an actual experiment (denoted "out"). Three values of ϕ_i^l have been investigated: 0°, 11° and 25°. The 0° angle corresponds to a case where only the geometrical roughness contributes to the resistance. One can note that a high capacity of shear resistance is obtained from this unique geometrical roughness, since a mobilized friction angle of 33° is found at peak. A difference between the results obtained from the measurements made at the global scale ("out") and the ones made in the first layer is obviously observed. This discrepancy was also reported by [40] in DEM CNL tests. Since local results are more valuable than the one derived from the outside, information extracted from the first layer is used for the identification of ϕ_i^l. A local friction angle of 25° is large enough to reach the expected behavior at the interface, i.e. a global friction angle of 37.7°.

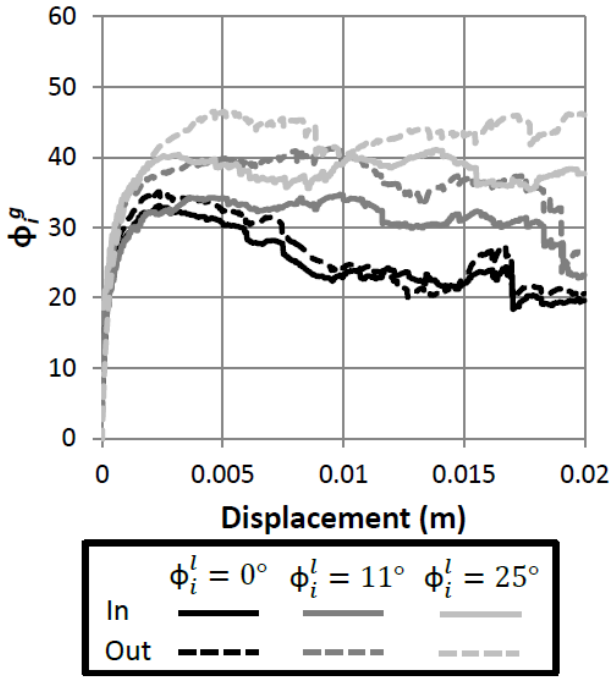

Figure 14: Evolution of the friction angle at interface during the CNL test.

One can note that the drop direction of the backfill grains is perpendicular to the wall face which is different from the method used on site. Further tests were performed with a drop direction parallel to the wall face. The discrepancy obtained was in the range of the dispersion of results inherent to the random nature of the sample.

The local parameters for the different sub-systems, wall, backfill and wall-backfill interface, are summarized in Table 1. The values corresponding to the friction angle between blocks and corresponding to different materials used in the full scale experiments by Villemus et al. [11] or Colas et al. [12] are given in Table 2.

Table 1: Values for the local and global parameters.

Sub-systems	**Global**	**Local**
Wall	$\phi_b{}^g$ = depending on the material (see Table 2)	Particle size: 8-11 mm Stiffness: 10^8 Pa/m Damping: $\zeta_n = 0.5$; $\zeta_t = 0.0$ $\phi_b{}^l = \phi_b{}^g$
Backfill	- $\phi_g{}^g = 37.7°$ - $\phi_{gc}{}^g \approx$ angle of repose $\rightarrow \phi_{gc}{}^g \approx 32°$	$AR = 2.5$ Particle size: 8-16 mm Stiffness: 5.10^7 Pa Damping: $\zeta_n = 0.5$; $\zeta_t = 0.0$ $\phi_g{}^l = 45°$ Porosity: $n_0 = 0.22$
Interface	Rough interface $\rightarrow \phi_i{}^g = 37.7°$	Stiffness: 5.10^7 Pa Damping: $\zeta_n = 0.5$; $\zeta_t = 0.0$ $\phi_i{}^l = 25°$

Table 2: Values of ϕ_b^g for the different stone wall materials.

Material	Global	
	Case A	**Case B**
Schist	28.5°	25°
Limestone	36°	35°

5. Modeling of DSRW

The DSRW loaded with a backfill is a quite complex system as it is composed of three mechanical sub-systems: the wall itself, the backfill and the backfill-wall interface. Therefore, we will first proceed with the validation of the modeling of the primary sub-system, the dry-stone wall itself. This case, denoted case A, corresponds to the full-scale experiments performed by Villemus et al. [11] where the walls were loaded with a hydrostatic load. In a second stage, the validation of full-scale experiments carried out by Colas et al. [12] is performed.

5.1 Loading: Hydrostatic load

To numerically build the wall, blocks are regularly constructed with a smooth joint contact law at their interface. The contact plane orientation follows the initial joint inclination α, i.e. collinear with α for the block-block interface between successive layers and perpendicular to α for the side-by-side blocks.

The first layer of blocks is fixed, consistent with the boundary condition used on site. The block dimension is 30 cm length and 12.5 cm height, each one is initially composed of about 470 disks. Figure 15 shows the wall model for wall V1L and V3L. We remind that the block model is rigid, this has been done to save computation time (a block is seen as a unique clump of particles instead of individual particles), and the block is transformed into a hollow block keeping the same mass: each block is then composed of 160 disks. Both models were created respectively with 7 089 disks and 27 400 disks.

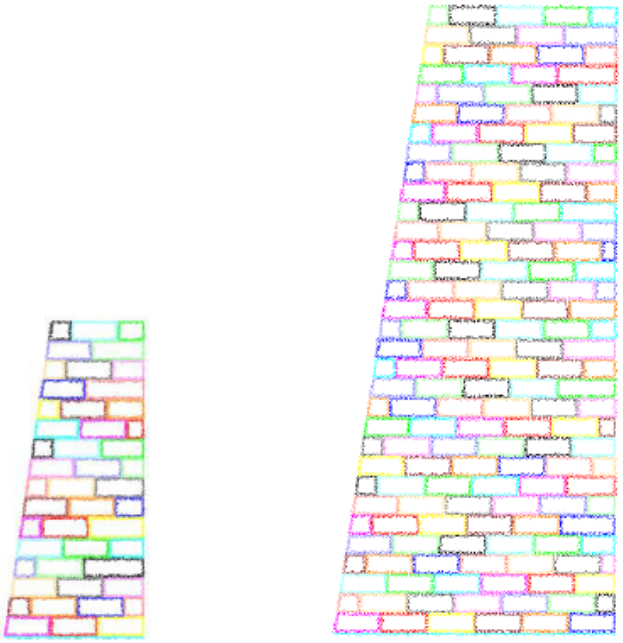

(a) (b)

Figure 15: Wall geometry of the case A simulations: (a) V1L (b) V3L.

The hydrostatic load is applied progressively (with an increment equals to 1% of the wall height) to disks at inward face, until the failure of the wall. At each increment, the particles on the inward wall face are detected. Then, the hydrostatic forces are evenly distributed among these particles following a triangular distribution. In this simulation, the inclination of the force vectors, which are initially strictly perpendicular to the inward wall face, is not modified throughout the simulation. In theory, when the wall inclined, a vertical component for the loading should be added to keep the loading vector perpendicular to the wall face. This simplification is nevertheless conservative.

In essence, two criteria are used to evaluate the stability of the walls. Knowing that the wall model is incrementally loaded, a criterion is used to know when the wall is stable enough before adding a new increment. This criterion is naturally based on the average unbalanced force criterion. Two different values have been used: (1) when the load height is less than 1 m (from $H_{cr}/2$ to $H_{cr}/3$), the model is assumed stable if the average unbalanced force is less than 10^{-2} N; (2) for the load height greater than 1 m, we use a more restrictive criterion, set to 10^{-3} N. Thus, the first half of simulations can be run faster.

If the first criterion is not met, we can suppose that the model is temporarily unstable or the model is already at failure. Then, a second criterion based on the kinetic energy is checked to evaluate the wall failure, or more precisely, to stop the simulation. The corresponding value was empirically calibrated on the basis of a numerical simulation involving the heaviest wall considered in the full scale experimental campaigns, i.e. wall V5S, which is also the highest. It is the one that is supposed to resist the greatest loading. The criterion that will be derived for stopping computations will be conservative for the other walls given that the damping coefficient at contacts between the individual objects is the same for all the studied cases.

We suppose that the model is already at failure if the wall kinetic energy is greater than 10^{-3} J/m during ten successive measurements (500 computation steps in between). These parameters were chosen based on the observation of the wall kinetic energy history. We can observe from Figure 16a that the kinetic energy rises considerably after each load increment, but is quickly dissipated as well. The required cycles to stabilize each load increment may vary, but the highly unstable window is very short, for example as shown in Figure 16a, it lasts less than 2500 computation steps (cycles).

At failure, the kinetic energy rises exponentially (Figure 16b). The mentioned critical kinetic energy of 10^{-3} J/m is then chosen based on several trial-and-error tests. Knowing that the largest wall (i.e. wall V5s) has a weight of approximately 7 ton/m; with a kinetic energy of 10^{-3} J/m, the wall at failure would move at 0.17 mm/s. This looks small as in reality the blocks may be displaced/rotated and find new configuration before failure due to a heterogeneous roughness between blocks. However the model does not accommodate this since the roughness is uniform and this criterion is appropriate strictly within the current numerical models.

Two different failure modes are produced from the simulation of the wall V1L and V3L (Figure 17). This figure corresponds to the wall deformed state when the kinetic energy criterion was reached.

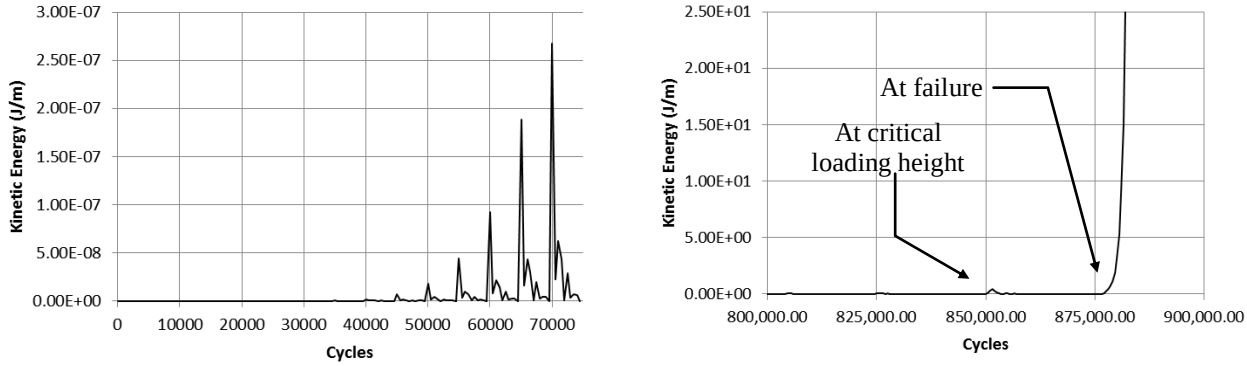

Figure 16: Kinetic energy history of wall V1L: (a) during the first fifteen load increments; (b) at few last increments before failure.

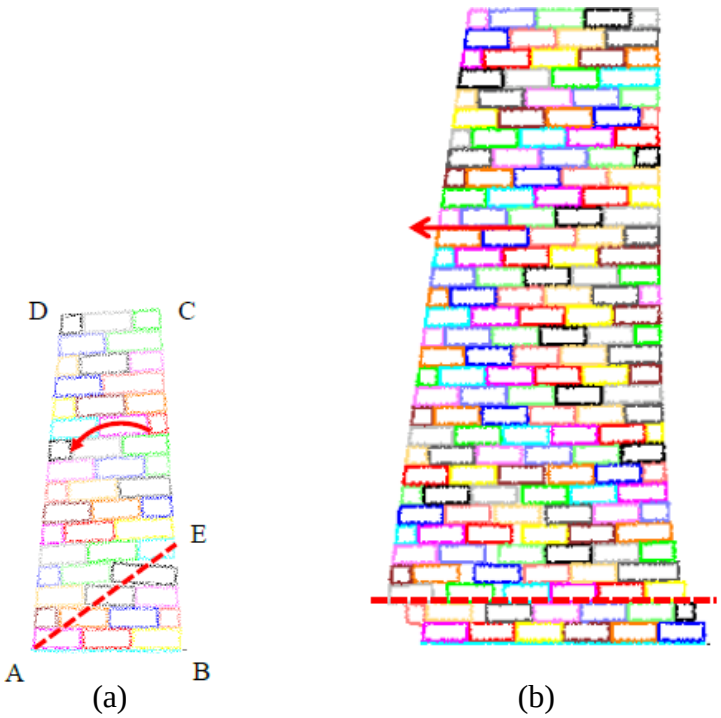

Figure 17: Plane strain failure: (a) Toppling (wall V1L) (b) Sliding (wall V3L).

The comparison between the DEM model (in terms of critical height) and the results from the experimental campaign for case A are shown in Table 3. From the simulations, we found a relative

error less than 9% with an uncertainty of ±0.5% corresponding to the load increment. This error is in the same range as the one found using the yield design method [17]. Nevertheless, not all the failure modes were retrieved by the simulations (Table 3). This difference may be contributed from simplifications in the modeling of a block shape. However, most probably this difference can be attributed to the assumption mentioned earlier: hydrostatic force vectors remain orthogonal to the initial inclination of inward wall face during the simulations. For an illustration, assume a total force F_t^{exp} was exerted in the slightly tilted experimental wall close to the failure, orthogonal to the inward wall face. In the DEM model, the same magnitude force F_t^{num} is also applied but strictly horizontal. The implications are as follow: (1) the component of F_t^{num} which is orthogonal to the inward wall surface has a smaller magnitude compared with F_t^{exp}, and (2) the tangential component to the wall is directed upward. To conclude, the first statement explains why the results of DEM modeling have generally a higher critical height compared to the experimental results (except for V4L wall). The second one explains that an extra uplift force contribute to the destabilization of the wall in the simulations, favoring a toppling mode.

The DEM models displacement histories for blocks at the top of the wall are shown in Figure 18a where h denotes the wall height and h_{water} the water height loading the wall. They can be compared to the experimental results shown in Figure 18b; these are the observation results from the highest installed displacement sensor (at ≈0.9h). We can note the following things: (1) they exhibit the same behavior: initially rigid and followed by a strong stiffness reduction close to failure; (2) the rigidity comparison between the experimental and numerical results are in good agreement: V2L wall is the most rigid and V5S is the less rigid. The V2L was the only wall built without the wall batter (λ_1=0°); this explains the rigid behavior of this wall. In contrast, the walls built with the biggest wall batter (λ_1=15°), i.e. V1L, V3L, V5S, produce a more deformable behavior. Among these three, V5S was also built with the biggest joint inclination (α=8.5°), thus it is able to deform more extensively compared to the other.

Table 3: Results for DEM simulations versus the experimental campaign for case A.

Wall height h (m)	2.0	1.95	4.0	2.0	4.25
Wall label	V1L	V2L	V3L	V4L	V5S
Experiment	1.74*S*	1.78*T*	3.37*S*	1.90*T*	3.62*S*
Numerical model (DEM)	1.89*T*	1.88*T*	3.54*S*	1.87*T*	3.77*T*
Relative error	9%	6%	5%	2%	4%

S = Sliding

T = Toppling

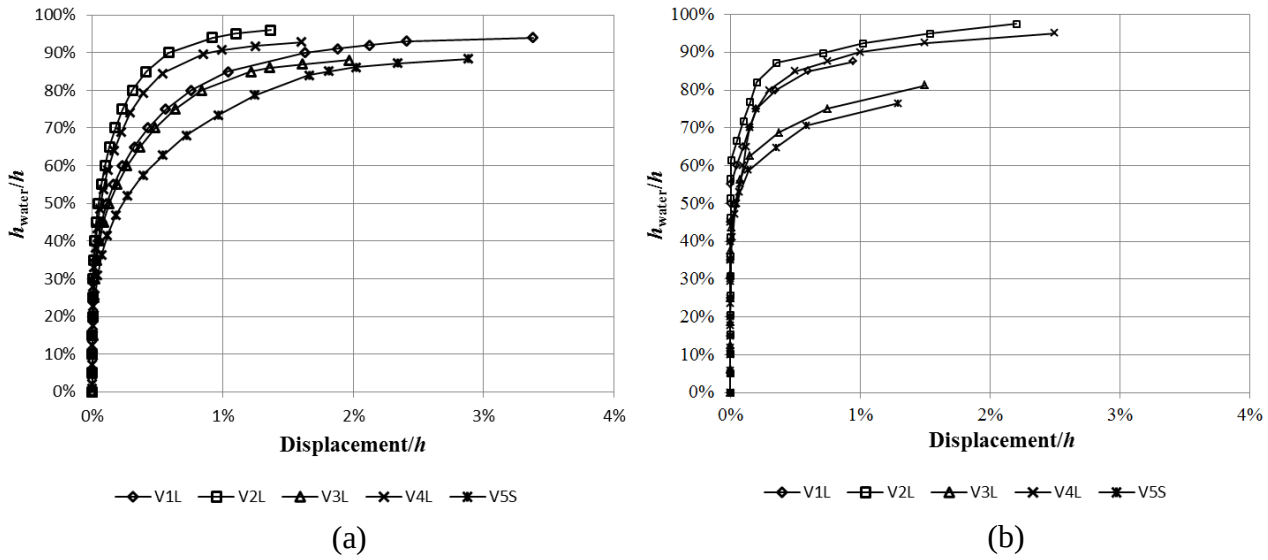

Figure 18: Relation between the normalized load (h_{water}/h) vs the normalized displacement of case A models: (a) DEM modeling; (b) experiment.

5.2 Loading: Backfill load

For case B wall models, walls are loaded by a backfill. Blocks size is 33 cm length and 12 cm height. Each hollow block consists of approximately 170 disks. In this case, the first layer of blocks is not fixed. However the foundation is fixed and modeled as a single layer of fixed disks. The friction angle between the first layer of blocks and the foundation is taken equal to the friction angle of a block-block interface. The full system loaded by the backfill is composed of about 65 000 disks.

The backfill is progressively created using layers thickness of ten centimeters. The layer thickness is then roughly equal to a wall block thickness. These grains were generated layer-by-layer and stabilized under gravity in a container of 2.5 m width. The friction angle between grains and the container wall is equal to the grain-grain local friction angle. The local parameters deduced in previous section was used here (Table 1). In order to reach an initial porosity of 0.22, a temporary local friction angle ϕ_g^l of 15.6° was set. Once the equilibrium is found, the local friction angle is reverted to 45°. Nevertheless, the temporary reduction of the local friction angle has an impact on the backfill slope. In fact, the angle of repose associated to the backfill slope decreased to a value lower than the angle observed on site. Consequently, the backfill slope is modified to the expected value (32°) before simulating a certain loading stage.

Similarly to the simulations with a hydrostatic load, two criteria were evaluated during the simulations. When the backfill height is less than 1.5 m (approximately $H_{cr}/2$), the system is classified as stable when an averaged unbalanced force is less than 5.10^{-2} N. When the backfill height is greater than 1.5 m, a more restrictive average unbalanced force is used (1.10^{-2} N). A less restrictive stability criterion is considered at the first part of the simulation to reduce time simulation: one single simulation takes about 17 days (on an Intel Xeon CPU 3.2GHz). The failure criterion (this is actually a termination criterion) is then checked when the stability criterion is not satisfied. This latter criterion is based on the kinetic energy evolution of the wall. If the wall kinetic energy during ten successive measurements is greater than 10^{-1} J/m, the wall is supposed to fail and the simulation is stopped.

This higher value for the critical kinetic energy criterion (as compared with the one in case A models) was selected to ensure that the simulation is not stopped before the visible failure shape has been obtained. More precisely the numerical time step in case A is 2.10^{-4} s, where the time step in case B simulations is much smaller at approximately $1.5.10^{-5}$ s, about one-tenth of case A simulations; hence in order to obtain the visible failure shape, case B requires far more cycles in comparison to the case A. One must note that actually the criterion used in the case A simulations may apply as well for case B simulations, but in that case one couldn't be certain that the failure has occurred.

The kinematic of blocks and grains velocity for wall C2s are shown in Figure 19b. We can distinguish two failure planes for the two different sub-systems (i.e. wall and backfill). Regarding the wall, one can observe that it is split into an immobilized bottom part and an overturned top part. This is typical of a toppling failure which is one of the two failure modes for slope retaining walls (Figure 3).

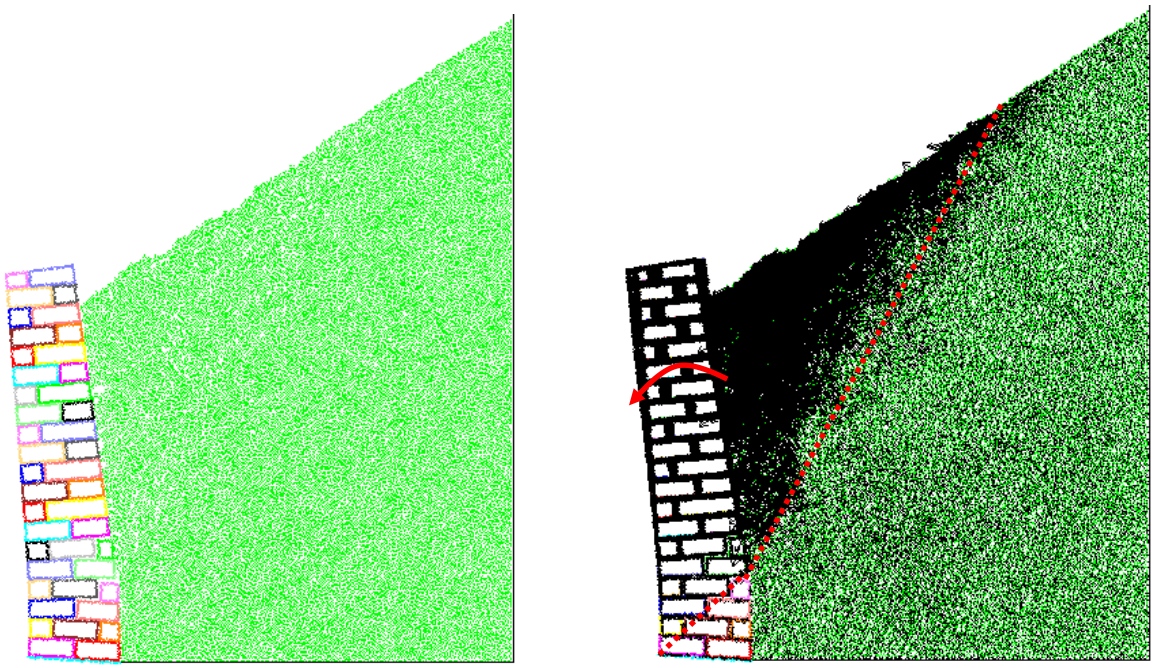

(a) (b)

Figure 19: Toppling failure in the wall C2S: (a) general view; (b) kinematic velocity field.

Table 4 shows the comparison between the results found throughout the numerical simulations and throughout the actual full scale experiments for case B. The creation of the numerical backfill is actually only one possible realization of a random process. The result in terms of critical backfill height (measured along the inward wall face) is given for two sets (two simulations) giving an idea of one's expectation about the representativeness of the computed critical height.

One can note that the critical height for case C3S and C4S is greater than the wall height itself. In those cases, a column of disks was created at the top-right part of the wall and fixed to the inward wall face. This was used to simulate the formwork (wood planks) added during the full scale experiments to increase the wall height. During the experiments of wall C3S and C4L, the effective failures were forced to occur by vibrating the lateral formworks. This has been done due to a blockage between the wall stones and the formworks, which happened at the final phase of the experimental test; supposedly because the tilted wall came into contact with the lateral formworks towards the final phase of loading. Nevertheless, before applying this vibration, both walls have

experienced a relatively large displacement at the top of the wall, about 8 cm for C3S and 5 cm for C4L [42]. These displacements remained relatively constant in the course of a 20 minutes pause. It may have induced a slight over prediction of the resistance of the actual walls. And therefore, this history may explain why the C3S and C4L simulations fail earlier than predicted from experimental results. In addition to, unlike in the numerical models, the added formwork in the experiments was not installed in such a way that its stability is warranted by the contact between the inward wall face and the backfill, but was supported at either side of the walls on the lateral formworks. Then the gravel that was subsequently poured acted on site like a uniform overload on the slope. In the case of the simulations, the load transfer to the wall was more direct.

Table 4: Results for DEM simulations versus the experimental campaign for case B.

Wall height h (m)	2.5	2.5	2.5
Wall label	C2S	C3S	C4L
Experiment	2.3S/T	2.78T	2.72T
Numerical model (DEM)	(1) 2.46T (2) 2.38T	(1) 2.68T (2) 2.72T	(1) 2.53T (2) 2.63T
Relative error	(1) 7% (2) 3%	(1) 4% (2) 2%	(1) 7% (2) 3%

S = Sliding

T = Toppling

For each wall case, the departure between the results from the numerical model and the experiments was found less than 10%. Nevertheless, the number of realization for a wall case is not high enough to have a clear insight on the reproducibility of the simulations.

Due to the high cost of a full scale experiment, no reproducibility test was carried out on site. Then, the error inherent to this kind of experiment is not accurately known which could help us to state about the validity of the fully DEM approach to model the behavior of a slope DSRW. Nevertheless, the range of error found through these six simulations can be compared to the one obtained by the yield design modelling [12,17,18] which was already validated by the comparison of the results provided by this latter method and those obtained with twelve full-scale experiments (and scale-down tests [15]). The range of error found with the DEM approach is approximately the same as or smaller than the one obtained by the yield design modelling. However, the DEM approach gives access to the deformation field which cannot provide the yield design method.

We give in Figure 20 the distribution of the horizontal and the vertical forces on the wall, at the critical backfill height, for case wall C2S. We can note the heterogeneity of the distribution where some blocks do not withstand any forces from the backfill. It evidences arching effects along the wall which are boosted by the rather high elongation ratio of the backfill particles.

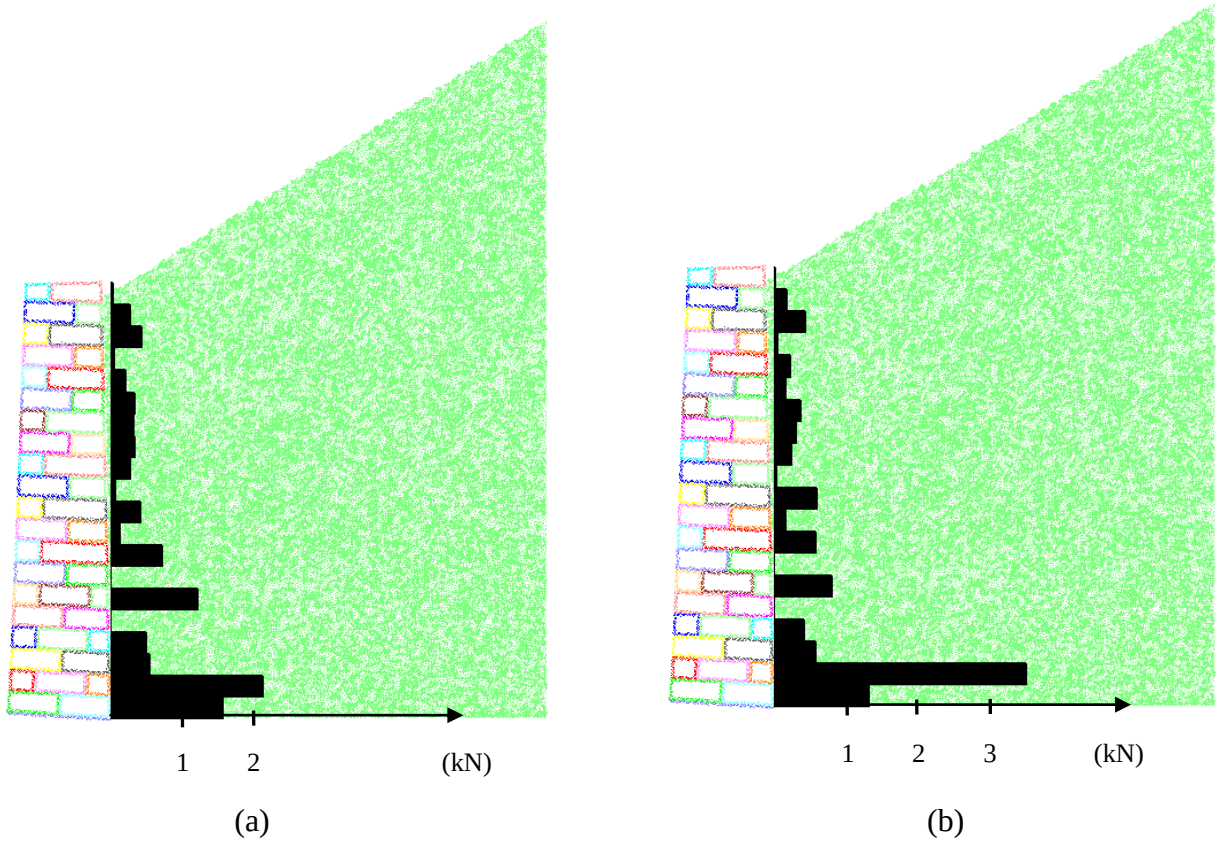

(a) (b)

Figure 20: Force distribution on the wall at critical height for wall C2S: (a) horizontal forces; (b) vertical forces.

The comparison between the displacement profiles obtained through the simulations and through the full scale of the experimental and numerical results is shown in Figure 21. The former one is fairly in a good agreement with the latter one, except when close to failure. This departure may be due to the fact that close to failure, a small load increment induces large displacements and a small error in the modeling is amplified at that computation stage.

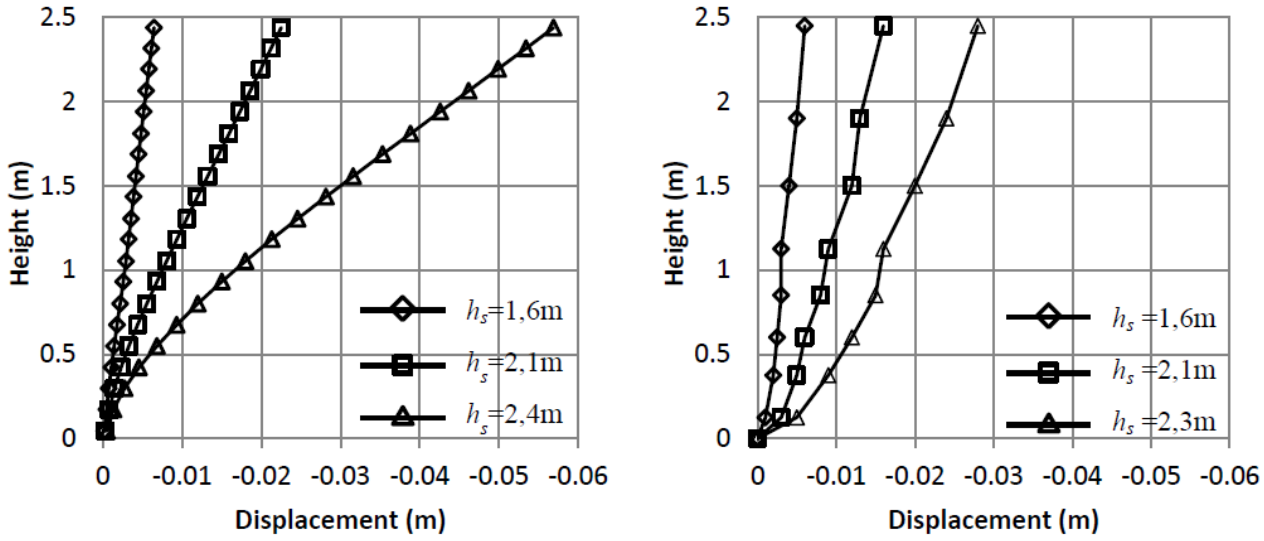

(a) (b)

Figure 21: Comparison of displacement profiles for wall C2S: (a) DEM modeling; (b) experiment.

6. Conclusions

In this work, a fully discrete model of the failure of DSRW was carried out and compared to full scale experiments. In the first stage, the validation of the method used for the creation of the wall was validated on the basis of full scale experiments where the walls were loaded by a hydrostatic pressure. The departure of the numerical results with respect to the experiments is in the same range as the one obtained by the Yield Design Method. In two cases, the sliding mode of failure was not found and may result from some simplifications regarding the modeling of the loading. In fact, the loading was not kept perpendicular to the inward wall face but set with a constant direction throughout the simulations.

In a second stage, a modeling of the failure of DSRW due to an excessive pressure induced by a backfill was performed. The simulation of three actual full scale experiments has been carried out. The technique to identify the local parameters which is complex in this case was given in details. The critical backfill heights found throughout the simulations were also in the same range as the ones obtained by the Yield Design Method. The hindsight on the validity of the Yield Design Method gives some clues about the validity of the fully DEM approach to model the behavior of slope DSRW in a correct way. However, the definite validity of this latter method is not so far stated and further work is required.

The fully DEM approach may be an oversized method since time computations are very important; nevertheless, it can be considered as the most refined approach as well for such problems. Moreover, this method gives access to the whole deformation field throughout loading and before failure which can be obtained by the Yield Design Method. This aspect was beyond the scope of this work and will be the subject of further publications.

7. Acknowledgement

The present work is part of the research projects C2D2 10 MGC S01 denoted PEDRA (Behavior of dry-stone or weakly bound structures) funded by the Ministry of Ecology (MEDDE) and the Civil and Urban Engineering Network (RGCU) and RESTOR (Restoration of Dry Stone Retaining Walls) funded by the Ministry of Culture (MCC) under the PNRCC program. The authors want to acknowledge these institutions for their support. The authors want also acknowledge the French Institute of Indonesia (Ministry of Foreign Affairs) for granting some extra funds for the PhD thesis of J. J. Oetomo.

8. References

1. Cundall PA, Strack ODL. A discrete numerical model for granular assemblies. Géotechnique 1979; 29(1), pp. 47-65, DOI: 10.1680/geot.1979.29.1.47.

2. Deluzarche R, Cambou B. Discrete numerical modelling of rockfill dams. International Journal for Numerical and Analytical Methods in Geomechanics 2006; 30(11), pp. 1075–1096, DOI: 10.1002/nag.514.
3. Plassiard JP, Donzé FV. Rockfall impact parameters on embankments: A Discrete Element Methods analysis. Structural Engineering International 2009; 19(3), pp. 333-341, DOI: 10.2749/101686609788957874.
4. Tang CL, Hu JC, Lin ML, Angelier J, Lu CY, Chan YC, Chu HT. The Tsaoling landslide triggered by the Chi-Chi earthquake, Taiwan: Insights from a discrete element simulation. Engineering Geology 2009; 106(1-2), pp. 1-19, DOI: 10.1016/j.enggeo.2009.02.011.
5. Alejano LR, Veiga M., Taboada J, Díez-Farto M. Stability of granite drystone masonry retaining walls: I. Analytical design. Géotechnique 2012; 62(11), pp. 1013-1025, DOI: 10.1680/geot.10.P.112.
6. Odent N. Recensement des ouvrages de soutènement en bordure du réseau routier national. Ouvrages d'art - centre des techniques d'ouvrages d'art 2000; 34, pp. 15-18.
7. O'Reilly MP, Bush DI, Brady KC, Powrie W. The stability of drystone retaining walls on highways. Proceedings of the ICE - Municipal Engineer 1999; 133(2), pp. 101-107, DOI: 10.1680/imuen.1999.31763.
8. Burgoyne J. Revetments of retaining walls. Corps of Royal Engineers Papers 1853; 3, pp. 154-159.
9. Harkness RM, Powrie W, Zhang X, Brady KC, O'Reilly MP. Numerical modelling of full-scale tests on drystone masonry retaining walls. Géotechnique 2000; 50(2), pp. 165-179, DOI: 10.1680/geot.2000.50.2.165.
10. Powrie W, Harkness RM, Zhang RM, Bush DI. Deformation and failure modes of drystone retaining walls. Géotechnique 2002; 52(6), pp. 435-446, DOI: 10.1680/geot.2002.52.6.435.
11. Villemus B, Morel JC, Boutin C. Experimental assessment of dry stone retaining wall stability on a rigid foundation 2007; 29(9), pp. 2124-2132, DOI: 10.1016/j.engstruct.2006.11.007.
12. Colas AS, Morel JC, Garnier D. Full-scale field trials to assess dry-stone retaining wall stability. Engineering Structures 2010; 32 (5), pp. 1215-1222, DOI: 10.1016/j.engstruct.2009.12.047.
13. Le HH. Stabilité des murs de souténement routiers en pierre sèche : Modélisation 3D par le calcul à la rupture et expérimentation échelle 1. PhD Thesis, ENTPE 2013.
14. Mundell C, McCombie P, Heath A, Harkness J, Walker P. Behaviour of drystone retaining structures. Proceedings of the ICE – Structures and Buildings 2010; 163(1), pp. 3-12, DOI: 10.1680/stbu.2009.163.1.3.
15. Colas AS, Morel JC, Garnier D. 2D modeling of a dry joint masonry wall retaining a pulverulent backfill. International Journal for Numerical and Analytical Methods in Geomechanics 2010; 34(12), pp. 1237-1249, DOI: 10.1002/nag.855.
16. Salençon J. Yield design. Wiley-ISTE: New Jersey, 2013.
17. Colas AS, Morel JC, Garnier D. Yield design of dry-stone masonry retaining structures – Comparisons with analytical, numerical, and experimental data. International Journal for Numerical and Analytical Methods in Geomechanics 2008; 32(14), pp. 1817-1832, DOI: 10.1002/nag.697.
18. Colas AS, Morel JC, Garnier D. Assessing the two-dimensional behaviour of drystone retaining walls by full-scale experiments and yield design simulation. Géotechnique 2013; 63(2), pp. 107-117, DOI: 10.1680/geot.10.P.115.

19. Claxton M, Hart RA, McCombie PF, Walker PJ. Rigid block distinct-element modeling of dry-stone retaining walls in plane strain. Journal of Geotechnical and Geoenvironmental Engineering 2005; 131(3), pp. 381-389, DOI: 10.1061/(ASCE)1090-0241(2005)131:3(381).

20. Walker P, McCombie P, Claxton M. Plane strain numerical model for drystone retaining walls. Proceedings of the ICE – Geotechnical Engineering 2007; 160(2), pp. 97-103, DOI: 10.1680/geng.2007.160.2.97.

21. Rothenburg L, Bathurst RJ. Micromechanical features of granular assemblies with planar elliptical particles. Géotechnique 1992; 42(1), pp. 79-95, DOI: 10.1680/geot.1992.42.1.79.

22. Ting JM, Meachum L, Rowell JD. Effect of particle shape on the strength and deformation mechanisms of ellipse-shaped granular assemblages. Engineering Computations 1995; 12(2), pp. 99-108, DOI: 10.1108/02644409510799497.

23. Nouguier-Lehon C, Vincens E, Cambou B. Structural changes in granular materials: The case of irregular polygonal particles. International Journal of Solids and Structures 2005; 42(24-25), pp. 6356-6375, DOI: 10.1016/j.ijsolstr.2005.04.021.

24. Azéma E, Radjaï F. Stress-strain behavior and geometrical properties of packings of elongated particles. Physical Review E 2010; 81, 051304, DOI: 10.1103/PhysRevE.81.051304.

25. Nouguier-Lehon C. Effect of the grain elongation on the behaviour of granular materials in biaxial compression. Comptes Rendus Mécanique 2010; 38(10-11), pp. 587-595, DOI: j.crme.2010.10.005.

26. Mas Ivars D, Potyondy D, Pierce M, Cundall P. The smooth-joint contact model. In: Proceedings of the 8th World Congress on Computational Mechanics and 5th European Congress on Computational Methods in Applied Sciences and Engineering, Venice, Italy 2008. Paper No. a2735.

27. Thornton C. Numerical simulations of deviatoric shear deformation of granular media. Géotechnique 2000; 50(1), pp. 43-53, DOI: 10.1680/geot.2000.50.1.43.

28. Yang ZX, Yang J, Wang LZ. On the influence of inter-particle friction and dilatancy in granular materials: a numerical analysis. Granular Matter 2012; 14(3), pp. 433-447, DOI: 10.1007/s10035-012-0348-x.

29. Tran TH. Analyse et modélisation du vieillissement des barrages en enrochement par une approche micromécanique. PhD Thesis, ECL 2006.

30. Salot C, Gotteland P, Villard P. Influence of relative density on granular materials behavior: DEM simulations of triaxial tests. Granular Matter 2009; 11(4), pp.221-236, DOI: 10.1007/s10035-009-0138-2.

31. Mirghasemi AA, Rothenburg L, Matyas EL. Influence of particle shape on engineering properties of assemblies of two-dimensional polygon-shaped particles. Géotechnique 2002; 52(3), pp. 209-217, DOI: 10.1680/geot.2002.52.3.209.

32. Mortara G, Mangiola A, Ghionna VN. Cyclic shear stress degradation and post-cyclic behaviour from sand-steel interface direct shear tests. Canadian Geotechnical Journal 2007; 44(7), pp. 739-752, DOI: 10.1139/t07-019.

33. Pra-ai S. Behaviour of soil-structure interfaces subjected to a large number of cycles: Application to piles. PhD Thesis, Université de Grenoble 2013.

34. Reyes SC, Iglesia E. Monte Carlo simulations of structural properties of packed beds. Chemical Engineering Science 1991; 46(4), pp. 1089-1099, DOI: 10.1016/0009-2509(91)85102-4.

35. Roblee LHS, Baird RM, Tierney, JW. Radial porosity variations in packed beds. AIChE Journal 1958; 4(4), pp. 460–464, DOI: 10.1002/aic.690040415.

36. Reboul N, Vincens E, Cambou B. A statistical analysis of void size distribution in a simulated narrowly graded packing of spheres. Granular Matter 2008; 10(6), pp. 457-468, DOI: 10.1007/s10035-008-0111-5.
37. Kishida H, Uesugi M. Tests of the interface between sand and steel in the simple shear apparatus. Géotechnique 1987; 37(1), pp. 45-52, DOI: 10.1680/geot.1987.37.1.45.
38. Fioravante V. On the shaft friction modelling of non-displacement piles in sands. Soils and Foundations 2002; 42(2), pp. 23-33, DOI: 10.3208/sandf.42.2_23.
39. Uesugi M, Kishida H. Influential factors of friction between steel and dry-sands. Soils and Foundations 1986; 26(2), pp. 33-46, DOI: 10.3208/sandf1972.26.2_33.
40. Zhang L, Thornton C. A numerical examination of the direct shear test. Géotechnique 2007; 57(4), pp. 343-354, DOI: 10.1680/geot.2007.57.4.343.
41. Itasca Consulting Group Inc. Particle Flow Code in 2 Dimensions: Theory and Background, Fourth Edition. Itasca: Minnesota, 2008.
42. Colas AS. Mécanique des murs de soutènement en pierre sèche: modélisation par le calcul à la rupture et expérimentation échelle 1. PhD Thesis, ENTPE 2009.